Ring-Resonator-Based Sub-THz Dielectric Sensor

Bo Yu, Xuan Ding, Hai Yu, Yu Ye, Xiaoguang Liu, and Qun Jane Gu

Abstract—This paper presents a design, fabrication, and measurement of a ring-resonator-based sub-THz dielectric sensor. The sensor consists of a ring resonator based notch filter, a sub-THz dielectric waveguide (DWG), and a pair of transitions from the microstrip line to the DWG. With low-loss and high permittivity silicon, the detected relative permittivity for materials is at the range of 1-11.9.

Index Terms—Dielectric sensor, dielectric waveguide (DWG), micromachining, notch filter, ring resonator, sub-THz, THz.

Fig. 1. (a) Schematic of the sub-THz dielectric sensor. (b) Magnitude of the *E*-field distribution of the dielectric sensor.

I. INTRODUCTION

DRIVEN by micromachining technology, sensing techniques become more and more attractive in applications of biology, medicine, pharma, food processing, and agriculture [1], [2]. One of the most popular techniques is the dielectric sensing by detecting the permittivity of a material. The sensing methods include reflection, transmission, and resonance. Both optical sensing, such as optical waveguide-based, fiber-based, and surface plasmon resonance-based sensors, and electrical sensing, such as capacitance-based, metallic waveguide-based sensors, have been investigated and demonstrated [3]–[8].

Recently, millimeter-wave and THz sensing applications, placed in a unique position in the electromagnetic spectrum, gain more attractions [9]. Since the sensing resolution requires more and more tiny and the corresponding operating wavelength is comparable with or even smaller than the millimeter wavelength. Moreover, the detected object with a sensitive permittivity property at this frequency range has more interactions with the peripheral objects. Therefore, sub-THz/THz sensors have huge potentials to provide solutions in many applications easily and cheaply to avoid complicated preparation processes and make the sensing technique time efficient and simple.

This paper presents a dielectric waveguide (DWG) ring-resonator-based sub-THz dielectric sensor. Since the DWG has an evanescent field in the surface of the ring resonator, it is sensitive to the effective permittivity change induced by the detected dielectric material. Due to the recycling nature of the ring associated with the DWG, the interactions between the resonator and the material are enhanced significantly. By leveraging the sub-THz frequency, the sensor size is reduced significantly compared with microwave sensors together with higher resolution. Besides, the low-loss high-resistivity silicon contributes to a high quality factor for high-sensitivity applications. In addition, this approach is compatible with the
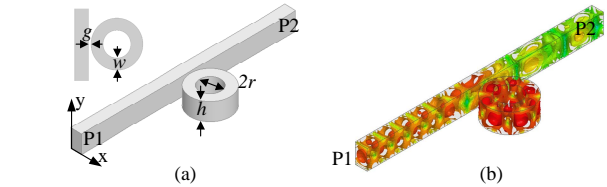
B. Yu, X. Ding, H. Yu, Y. Ye, X. Liu, and Q. J. Gu are with the Department of Electrical and Computer Engineering, University of California, Davis, CA, 95616, USA (e-mail: boyu@ucdavis.edu; xxding@ucdavis.edu; jetyu@ucdavis.edu; yuye@ucdavis.edu; lxgliu@ucdavis.edu; jgu@ucdavis.edu)

planar silicon fabrication processes and has the potentials to integrate with active integrated circuits for small form factor sensors with low costs. Therefore, the DWG ring-resonator-based sensor structure has potential features of high resolution, small size, and low cost for wide deployments.

II. DESIGN OF SUB-THz DIELECTRIC SENSOR

Dielectric materials have two properties, dielectric constant ε_r and loss tangent $\tan\delta$, which can be detected by a resonance-based sensor based on the shift of the resonant frequency f_r and the change of the quality factor Q. f_r is written as

$$f_r = \frac{mc}{2\pi r \sqrt{\varepsilon_{\text{reff}}}}, \tag{1}$$

where m is a positive integer, c denotes the speed of light, r denotes the ring radius, and $\varepsilon_{\text{reff}}$ denotes the effective relative ε_r, which is related to the ring width w, the ring height h, and the sensed material ε_r. When the sensed material is put close to the resonator, $\varepsilon_{\text{reff}}$ increases and then f_r decreases. By checking frequency shift, ε_r is detected. Due to the loading effect, Q is affected by the sensed material. Hence, the loaded Q is formulated by

$$\frac{1}{Q_{\text{loaded}}} = \frac{1}{Q_{\text{Si}}} + \frac{1}{Q_{\text{rad}}} + \frac{1}{Q_{\text{scatter}}} + \frac{1}{Q_{\text{SM}}}, \tag{2}$$

where Q_{Si} and Q_{SM} denote the quality factors related to material losses of the DWG resonator and the sensed material, respectively, Q_{rad} denotes the quality factor related to the radiation loss due to the ring size and the nonideal fabrication, and Q_{scatter} denotes the quality factor related to the scattering loss due to the surface roughness.

The schematic of the proposed dielectric sensor is illustrated in Fig. 1(a). It consists of a straight DWG and a ring-shaped resonator. Since the ring resonator is adjacent to the straight DWG, the signals at f_r will be trapped in the ring without transmission and reflection. Fig. 1(b) shows the simulated magnitude of the *E*-field distribution at f_r.

f_r is majorly determined by r and $\varepsilon_{\text{reff}}$ as (1) indicated. When r increases, the total equivalent circle length increases, and then f_r decreases; when w or h increases, $\varepsilon_{\text{reff}}$ increases, and then f_r decreases too. A two-port Q, which is related to not

only the loaded quality factor Q_{loaded} but also the coupling coefficient k between the ring and the DWG, is employed to evaluate the sensed material loss tangent $\tan\delta_{\text{SM}}$. k is related to g, r, w, and h. Fig. 2 plots f_r, and Q versus g, r, w, and h, respectively. For the shunt resonator, under-coupling results that the resonator is bypassed and over coupling results that the trapped signals on the ring are coupled back. Since w, h are linked with the mode and the cutoff frequency f_c of the DWG, r and g are used to determine f_r and Q, respectively. The sensitivity and the resolution of ε_r can be formulated as

$$\text{sen}_{\varepsilon_r} = \frac{\partial f}{\partial \varepsilon_r}\Big|_{f=f_{r0}} \quad (3)$$

and

$$\text{rsltn}_{\varepsilon_r} = \frac{\Delta f_{\min}}{\text{sen}_{\varepsilon_r}}\Big|_{f=f_{r0}} \propto \frac{1}{Q_S}\frac{\partial \varepsilon_r}{\partial f}, \quad (4)$$

where $\Delta f_{\min}$ denotes the system minimum detectable frequency shift, which is determined by the clock phase noise of the detection system and inversely proportional to the system Q_S, and f_{r0} denotes the unloaded f_r. The bandwidth broadening is determined by $\tan\delta_{\text{SM}}$. The corresponding sensitivity and resolution can be formulated as

$$\text{sen}_{\tan\delta} = \frac{\partial Q_{\text{loaded}}}{\partial \tan\delta_{\text{SM}}} = -C_2 Q_{\text{loaded}}^2 \quad (5)$$

and

$$\text{rsltn}_{\tan\delta} = \frac{\Delta \text{BW}_{\min}}{\text{sen}_{\tan\delta}} = -\frac{\Delta \text{BW}_{\min}}{C_2 Q_{\text{loaded}}^2}, \quad (6)$$

where $\Delta \text{BW}_{\min}$ denotes the minimum detectable bandwidth change of the detection system, and C_2 is the coefficient of $\tan\delta_{\text{SM}}$. Both resolutions will be boosted by increasing quality factors. Besides, sensing location is critical. The more interactions between the ring and the sensed material, the higher the sensitivity is. The sensed materials put in different sensitive locations are evaluated in Fig. 3(a)-(c), and the corresponding $\text{sen}_{\varepsilon_r}$ are 2.9 GHz, 2.0 GHz, and 0.4 GHz, respectively, as shown in Fig. 3(d). Due to the bending radiation, the ring outside is the most sensitive location. The ring top and bottom sides are more sensitive than the ring inside. Considering the preparation easiness, the sensed material with the square shape is selected. The calculated and simulated Q_{loaded} versus $\tan\delta_{\text{SM}}$ are plotted as shown in Fig. 3(e). When the loss is dominated by the sensed material, $\tan\delta_{\text{SM}}$ sensitivity is about a constant, which is 1.7×10^4 when $\tan\delta_{\text{Si}} = 0.002$.

Referring to [10], 165 GHz is selected as the unloaded operating frequency and the corresponding w and h are equal to 300 and 500 μm, respectively. To minimize the sensor size, $m = 3$ due to f_c of 120 GHz and $r \approx 260$ μm. For the highest Q, g is optimized as 50 μm.

Considering the planar integration, the microstrip line (MSL)-to-DWG transitions are employed [11]. Besides, to facilitate the test, GSG-to-MSL transitions are used. To balance the structure, a double-ring sensor is designed instead of the single one. To compatible with the fabrication, the octagon shape for the sensor is employed instead of the ring shape. In addition, to control g and support a reliable fabrication, four anchors are used to connect the ring and the straight DWG.
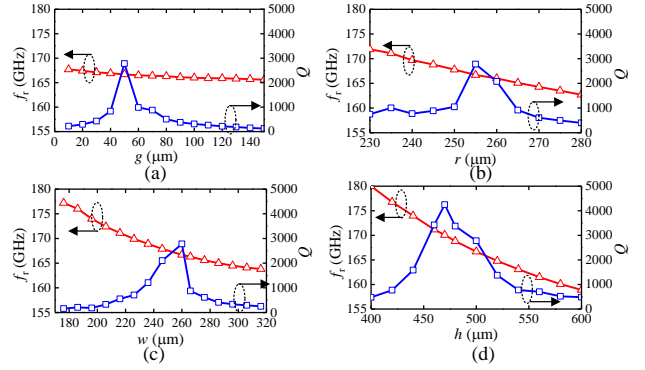

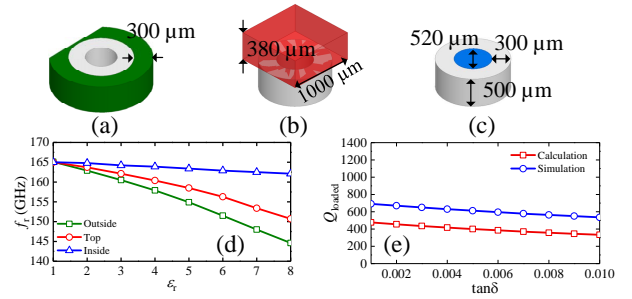Fig. 2. (a) f_r and Q versus (a) g, (b) r, (c) w, and (d) h for the unloaded resonator with the DWG.

Fig. 3. Sensing location: (a) Outside of the ring, (b) Top of the ring, and (c) Inside of the ring. (d) Simulated f_r versus the relative ε_r with the sample in the different locations. (e) Calculated and simulated Q_{loaded} versus $\tan\delta_{\text{SM}}$.

The schematic of the integrated double-ring sub-THz dielectric sensor is shown in Fig. 4.

III. SIMULATION AND MEASUREMENT RESULTS

The sub-THz dielectric sensor is fabricated by the deep reactive ion etching (DRIE) process and the transition board is fabricated by the liftoff process [11]. With the prepared dielectric sensor and the transition board, a pick-and-place tool (Finetech Fineplacer PICO A4) is used to bond the sensor on the transition board with a thin BCB layer. The device photos are shown in Fig. 5(a) and (b). The total size of the OMT channel is 20 mm $\times$ 6.3 mm with a 10-mm straight DWG. Fig. 5(c) illustrates the side view of the testbench [11]. To reduce the interference from the chunk metal of the test bench, the sensing area is lifted up by two pieces of 1-mm glass.

To calibrate the measurement, commercial dielectric materials, including Rogers 5880, TMM3, TMM4, and TMM6, are used. Prepared by a dicing saw with the blade width of 80 μm, the sensed materials are diced into 1 mm $\times$ 1 mm $\times$ 0.38 mm. The simulated and measured S_{21} versus frequency are plotted
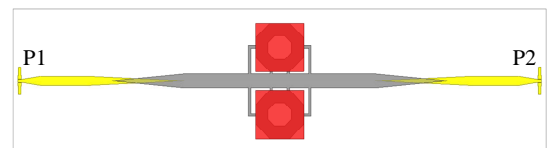

Fig. 4. Schematic of the integrated double-ring sub-THz dielectric sensor.
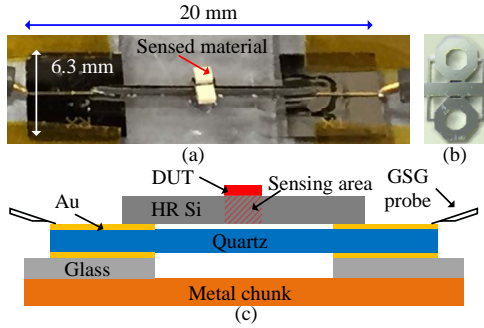
Fig. 5. Photographs of (a) Integrated double-ring sub-THz dielectric sensor, and (b) Zoomed-in rings. (c) Illustration of the side view of the test bench.
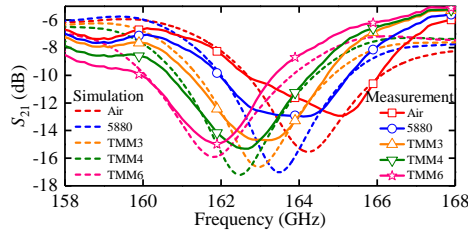

Fig. 6. Simulated and measured S_{21} with commercial 1 mm $\times$ 1 mm $\times$ 0.38 mm dielectric materials, including Rogers 5880, TMM3, TMM4, and TMM6.

in Fig. 6. The estimated relative dielectric constants are 2.6, 3.1, 4.5, and 6.0, respectively, and the estimated loss tangents are 0.01, 0.03, 0.01, and 0.006, respectively. Considering the transition interface flatness, the simulations for the TMM4 and the TMM6 are with 10- and 15-μm air-gaps, which are correlated by simulation, respectively. The measured sen$_{\varepsilon r}$ and rsltn$_{\varepsilon r}$ are 0.6 GHz and 1.7 $\times$ 10^{-6}, respectively.

The decrease of the sensitivity is dominated by the air-gap effect since $\varepsilon_{\mathrm{reff}}$ is decreased. To analyze the air-gap effect, S_{21} versus frequency with the various air-gaps are plotted in Fig. 7(a), and f_r and Q versus the air-gap are plotted in Fig. 7(b). Except for the air-gap effect, the positioning error, the size error could also degrade the measurement accuracy. However, when the sensed material size error is less than 20 μm, the thickness is larger than 200 μm, and the placement offset is less than 200 μm, the effects are negligible.

After the calibration, several materials, including paper, red rubber, black rubber, and glass, are sensed. The simulated and measured S_{21}s are shown in Fig. 8. The estimated dielectric constants are 2.3, 3.2, 4.4, and 7.0, respectively, and the estimated loss tangents are 0.42, 0.5, 0.5, and 0.1, respectively. Table I summarizes the performance comparison with the
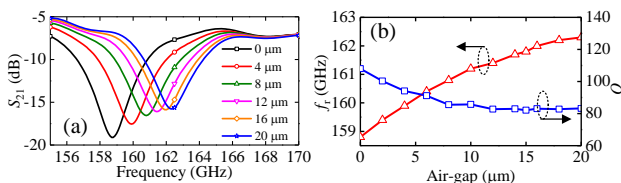

Fig. 7. (a) Simulated S_{21} versus frequency. (b) Simulated f_r and Q versus the air-gap.
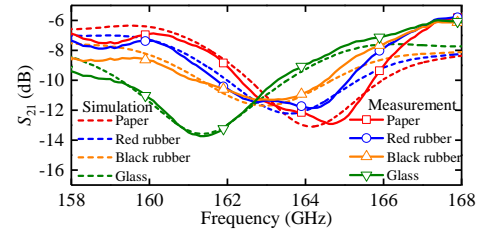

Fig. 8. Measured S_{21} with some practical dielectric materials, including paper, red rubber, black rubber and glass.

TABLE I
DIELECTRIC SENSORS COMPARISON

Design	[2]	[6]	[8]	Proposed
Method	Resonance	Resonance	Reflection	Resonance
Operating frequency	193 THz	10 GHz	2.5 GHz - 6.5 GHz	165 GHz
ε_r sensitivity	14.1 THz	0.022 GHz	N/A	0.6 GHz
ε_r resolution	1.1×10^{-4}	$4.5 \times 10^{-5}*$	N/A	$1.7 \times 10^{-6}*$
Material size	Small	Large	Large	Moderate
Planar integration	Hard	Hard	Hard	Easy

* Assume Δf_{min} = 1 kHz

recently published dielectric material sensors.

IV. CONCLUSION

The proposed sub-THz dielectric sensor is aimed to characterize and sense different dielectric materials, and eventually can be applied to biology, medicine, pharma, food processing, agriculture, and so on. In addition, the sensor design methodology can be readily applied to higher frequencies in the THz range.

REFERENCES

[1] K. Ajito and Y. Ueno, "THz chemical imaging for biological applications," *IEEE Trans. THz Sci. Technol.*, vol. 1, no. 1, pp. 293-300, Sep. 2011.

[2] T. Claes *et al.*, "Label-free biosensing with a slot-waveguide-based ring resonator in silicon on insulator," *IEEE Photonics J.*, vol. 1, no. 3, pp. 197–204, Sep. 2009.

[3] A. Ksendzov and Y. Lin, "Integrated optics ring-resonator sensors for protein detection," *Opt. Lett.*, vol. 30, no. 24, pp. 3344–3346, Dec. 2005.

[4] M. Chamanzar, *et al.*, "Hybrid photonic surface-plasmon-polariton ring resonators for sensing applications," *Appl. Phys. B*, vol. 101, no. 1-2, pp. 263–271, Oct. 2010.

[5] M. R. Foreman, J. D. Swaim, and F. Vollmer, "Whispering gallery mode sensors," *Adv. Opt. Photonics*, vol. 7, no. 2, pp. 168–240, Jun. 2015.

[6] R. Ramzan, M. Omar, and O. F. Siddiqui, "Energy-tunneling dielectric sensor based on substrate integrated waveguides," *IEEE Sens. J.*, vol. 17, no. 5, pp. 1264–1268, Mar. 2017.

[7] D. Maji *et al.*, "ClotChip: a microfluidic dielectric sensor for point-of-care assessment of hemostasis," *IEEE Trans. Biomed. Circuits Syst.*, vol. PP, no. 99, pp. 1–11, 2017.

[8] S. Julrat, S. Trabelsi, and S. O. Nelson, "Open-ended half-mode substrate-integrated waveguide sensor for complex permittivity measurement," *IEEE Sens. J.*, vol. 18, no. 7, pp. 2759–2767, Apr. 2018.

[9] G. Annino *et al.*, "Dielectric properties of materials using whispering gallery dielectric resonators: Experiments and perspectives of ultra-wideband characterization," *J. Chem. Phys.*, vol. 112, no. 5, pp. 2308–2314, Jan. 2000.

[10] B. Yu, *et al.*, "High-efficiency micromachined sub-THz channels for low-cost interconnect for planar integrated circuits," *IEEE Trans. Microw. Theory Tech.*, vol. 64, no. 1, pp. 96–105, Jan. 2016.

[11] B. Yu *et al.*, "Low-loss and broadband G-band dielectric interconnect for chip-to-chip communication," *IEEE Microw. Wirel. Compon. Lett.*, vol. 26, no. 7, pp. 478–480, Jul. 2016.